Feature-Adaptive Motion Tracking of Ultrasound Image Sequences Using A Deformable Mesh

Fai Yeung, Stephen F. Levinson,* *Member, IEEE*, Dongshan Fu, and Kevin J. Parker, *Fellow, IEEE*

Abstract—By exploiting the correlation of ultrasound speckle patterns that result from scattering by underlying tissue elements, two-dimensional tissue motion theoretically can be recovered by tracking the apparent movement of the associated speckle patterns. Speckle tracking, however, is an ill-posed inverse problem because of temporal decorrelation of the speckle patterns and the inherent low signal-to-noise ratio of medical ultrasonic images. This paper investigates the use of an adaptive deformable mesh for nonrigid tissue motion recovery from ultrasound images. The nodes connecting the mesh elements are allocated adaptively to stable speckle patterns that are less susceptible to temporal decorrelation. We use the approach of finite element analysis in manipulating the irregular mesh elements. A novel deformable block matching algorithm, making use of a Lagrange element for higher-order description of local motion, is proposed to estimate a nonrigid motion vector at each node. In order to ensure that the motion estimates are admissible to a physically plausible solution, the nodal displacements are regularized by minimizing the strain energy associated with the mesh deformations. Experiments based on ultrasound images of a tissue-mimicking phantom and a muscle undergoing contraction, and on computer simulations, have shown that the proposed algorithm can successfully track nonrigid displacement fields.

Index Terms—Deformable mesh, finite element analysis, non-rigid motion estimation, ultrasound images.

I. INTRODUCTION

ULTRASOUND images of soft tissues are characterized by a granular pattern known as speckle in analogy to the optical speckle observed with lasers. Given a stable scattering structure, ultrasound speckle is deterministic and is temporally stable for small tissue motions. The temporal correlation of ultrasound speckle provides a basis for the recovery of tissue motion by tracking the apparent movement of the associated speckle patterns, when motions are in plane and are small.

Speckle tracking represents a promising development in ultrasound imaging due to its potential advantages over one-dimensional (1-D) ultrasound Doppler techniques [1]. It has been applied in a variety of biomedical applications, including the use of an optical flow technique to assess local myocardial deformation [2], and the use of a block matching algorithm for blood flow assessment [3] and to derive tissue elasticity information [4].

Unfortunately, the existing techniques are largely based on motion estimation algorithms developed for digital video. Despite similarities in the motion recovery problem for both visual scene-oriented and ultrasonic medical images, the image and motion models in the two types of images and, hence, the strategies of motion estimation, differ from each other in various aspects. A comparison of scene-oriented and ultrasonic image sequences is summarized in Table I.

A. Challenges in Speckle Tracking

The inverse problem of motion recovery from ultrasonic image sequences poses a significant challenge. The challenges in speckle tracking are discussed as follows.

- *Tissue deformation*: Tissue motion consists not only of translation and rotation but also deformation. Tissue deformation requires a higher-order local description.
- *Noisy images*: Ultrasonic medical images have a low signal-to-noise ratio (SNR). The images are characterized by Rayleigh-governed speckle noise and corrupted by Gaussian-distributed electronic noise.
- *Motion ambiguities*: The spatial and temporal changes of a speckle pattern can be quantified and derived with local operators that compute the spatial and temporal derivatives or match similarities in two frames. Ambiguities arise when there is insufficient representation of spatial information, e.g., in regions of image saturation or specular reflection or homogeneous regions of weak acoustic scatterers.
- *Spatial aliasing*: Because of similarities shared among different speckle patterns, spatial aliasing is likely to occur if the tissue displacement is large compared to the size of the speckle cell, resulting in false matches or incorrect estimates of gradients.
- *Speckle decorrelation*: Since speckle patterns result from the constructive and destructive interference of ultrasonic echoes from numerous subresolvable elements, nonuniform movement of these scatterers in the insonified tissue volume can cause temporal decorrelation of the speckle patterns. The problem of speckle decorrelation is especially prominent in regions with weak or diffuse scatterers.

TABLE I
COMPARISON OF SCENE-ORIENTED AND ULTRASONIC IMAGE SEQUENCES

	Visual Scene Image Sequence	Ultrasound Image Sequence
Image capture	Camera	Ultrasound scanner
Image plane	Perspective projection of 3-D objects	Cross section of 3-D tissue structures
Intensity function	Smooth, slow varying across objects	Speckle-like pattern, rapidly varying
Motion types	Translation + rotation rigid	Translation + rotation + deformation
Typical resolution	Pixel resolution (approx.)	Pulse dimension resolution
Challenges	Changes in external illumination, occlusion, aperture problems, no gray value changes	Low SNR, speckle decorrelation, motion ambiguities, spatial aliasing

- *Out-of-plane motion*: Current state-of-the-art clinical ultrasound scanners are limited to imaging cross-sections of three-dimensional (3-D) tissue structures. This restricts the application of speckle tracking to the recovery of a two-dimensional (2-D) motion field only. Furthermore, out-of-plane motion can cause decorrelation of speckle patterns from the diffraction pattern of the ultrasound pulse in the elevational direction.
- *Speckle motion artifacts*: Speckle motion artifacts generally refer to apparent speckle motion inherent to the image formation process itself. A good example of this is the speckle rotation artifact [5] in which the apparent speckle motion consists of the actual tissue motion plus a strong translational component resulting from the curvature of the system point spread function. Signal reverberation [6] resulting from multiple reflections from specular structures may also produce false signals that are difficult to handle by image processing means, but that often can be eliminated manually by adjusting system parameters.
- *Quantization error*: Quantization errors in speckle tracking result from the discretization of the intensity function and from the measurement of displacement vectors in discrete steps.

Most problems in ultrasonic speckle tracking are related to either an incomplete coupling or a decoupling of image information from that of the underlying tissue. Among them, speckle decorrelation has the most profound effect on the accuracy of motion estimates since speckle tracking algorithms depend on the stability of the speckle pattern. Understanding these problems may make it possible to develop better strategies for motion tracking.

B. A New Approach to Speckle Tracking

Our goal was to devise a motion estimation algorithm that is sufficiently robust to be suitable for ultrasonic speckle tracking of soft tissue motion. The first step toward accurate motion estimation is to extract features from speckle patterns that are stable with the underlying tissue motion. This requires *a priori* knowledge of ultrasound speckle models. The speckle pattern resulting from the presence of numerous weak scatterers is generally governed by Rayleigh statistics [7]. In this case, the speckle has a constant contrast (SNR = 1.91) and a fixed speckle cell size related only to the system point-spread-function of the ultrasound scanner. In other words, the first- and second-order speckle statistics do not carry any signature

information from the tissue itself. On the other hand, speckle patterns that result from periodic strong scatterers appear to be brighter, larger, and more structural than speckle patterns from diffuse scattering. These structural speckle patterns in the ideal case are temporally stable under conditions of small tissue motion.

In order to capture temporally stable speckle features, a feature energy function has been formulated that consists of a sum of oriented band-passed decompositions of ultrasound images using multichannel filters. A quadrilateral mesh is then generated by assigning mesh nodes adaptively to places of high feature energy, and motion vectors are estimated only at those nodes. The motion estimates should be more reliable by tracking speckle patterns that are less susceptible to temporal decorrelation. Manipulation of the irregular mesh elements is accomplished through the application of finite element analysis (FEA). FEA provides a convenient mathematical tool that allows the construction of a novel deformable block matching algorithm. The algorithm involves the mapping of an irregular mesh element to a regular parent element using a Lagrange element for higher-order description of local motion. Because the mapping compensates for local tissue deformations, a traditional block matching algorithm that assumes motion rigidity can then be applied to estimate local motion vectors.

The effect of speckle decorrelation on motion tracking is further reduced by using a regularization method, as demonstrated in [8]. Specifically, the speckle tracking problem is formulated as a conservative dynamic system in which the motion solution results from the minimization of two energy functions. The first energy function is a similarity measure. The second function is based on the strain energy of the mesh elements, which acts as a stabilizing functional to ensure that the motion estimates are admissible to a physically plausible solution.

II. ADAPTIVE DEFORMABLE MESH

In general, a mesh is a partition of an image domain into polygonal elements. Motion vectors are estimated only at the nodal points where the mesh elements intersect. The generation of a feature-adaptive hierarchical mesh is accomplished in two steps. First, features of the speckle patterns that are temporally stable are extracted. Next, an hierarchic mesh is generated adaptively by allocating nodes to regions of high feature energy and dividing those mesh elements that have a high intraelemental feature energy into finer elements.
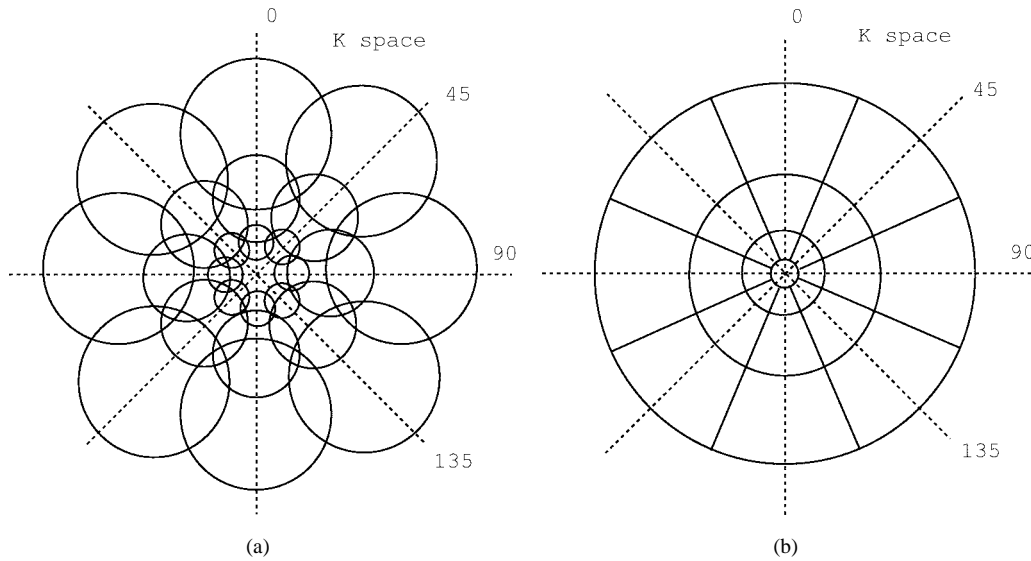
Fig. 1. Diagram of frequency responses of (a) Gabor filters. (b) Diagram of idealized frequency responses of the steerable wavelet pyramid. The frequency domain of an image in both diagrams is divided into subbands of three scale levels and orientations at 0°, 45°, 90°, and 135°.

A. Feature Extraction

Features such as scale and orientation of speckle patterns are obtained from subband decomposition of ultrasound images using multichannel bandlimited and directional filters. Two such filters are Gabor wavelet filters [9] and the steerable wavelet pyramid [10]. Fig. 1 compares the directional spatial frequency responses of the two filters. Scale and orientation information from the separate outputs of subband decomposition are used to facilitate feature extraction. In doing so, the outputs of subband decomposition are used to form a composite feature energy map C_f, which is a sum of the energy of bandpass filter outputs P_{so}

$$C_f(\boldsymbol{x}) = \sum_{s=1}^{3} \sum_{o=0}^{3} P_{so}^2(\boldsymbol{x}) \qquad (1)$$

where s and o are the indexes of scale and orientation, respectively, and $P_{so}^2(\boldsymbol{x})$ is the energy of the filter outputs. Note that the low-pass (inner portion of the filter diagrams) and high-pass (outer portion of the filter diagrams) energy bands of the image are not used in the feature composition because they contain little useful information for characterization of speckle patterns. Ideally, the center frequency of the bandpass (middle portion) energy band should be chosen to correspond to the spatial frequency of anatomical tissue features (e.g., muscle fascicles).

Fig. 2 shows a B-scan of a human forearm that contains groups of muscles overlying a bone, the *ulna*, along with the corresponding composite feature map. As can be seen, the feature map emphasizes regions of highly structural content and de-emphasizes homogeneous regions such as the region at the left of the image and the bone at the bottom.

B. Feature-Adaptive Mesh Design

The generation of a feature-adaptive mesh begins with the allocation of nodes using the composite feature energy map. Ideally the nodes should be distributed more or less
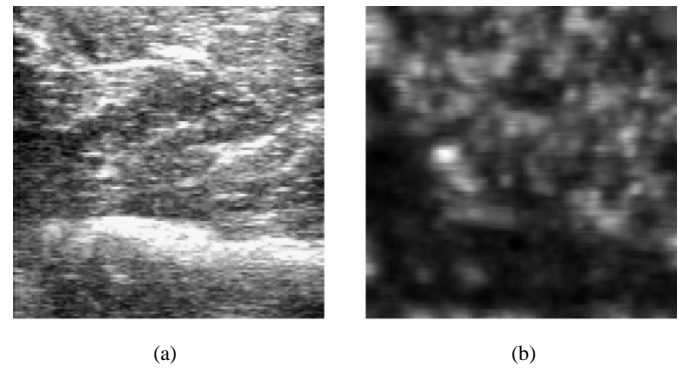

Fig. 2. (a) An ultrasound image and (b) its corresponding composite feature map. The size of the region of interest is 100×100 pixels, or 2.5×2.5 cm^2.

uniformly within the region of interest. Although a regular grid could easily be superimposed on the image, the nodes would not necessarily correspond to the regions of highest feature energy. In order to place the nodes appropriately, the nodes are considered to be connected by elastic springs. A load is applied to each node consisting of an attractive force that acts to move the node to the vicinity of areas of high feature energy. We start by placing a uniformly spaced rectangular grid over the region of interest of the image plane. The potential energy at node m, $\mathcal{E}_m$, is a combination of the internal spring restoration energy $\mathcal{E}_s$ and the feature energy possessed by the applied load $\mathcal{E}_f$

$$\mathcal{E}_m = \mathcal{E}_s + \mathcal{E}_f = \tfrac{1}{2} k\varepsilon^2 - \tfrac{1}{2} c_f D^2 \qquad (2)$$

where ε^2 at each node is the total sum of the squared length changes of the springs connected to the node $\varepsilon^2 = \sum_{i=1}^{4} d_i^2$, k is the spring constant, c_f is the composite feature energy at the nodal position in the unstretched configuration, and $\|D\|^2$ is the squared magnitude of the nodal displacement vector. The length change d_i is expressed as the difference of the rest length L and the stretched length l_i, i.e., $d_i = l_i - L$. In the mesh design it is assumed that all springs are identical so that they have the same spring constant. The choice of the spring
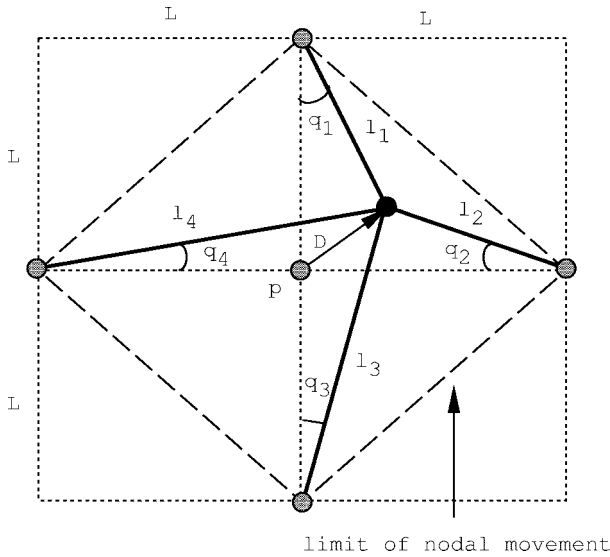
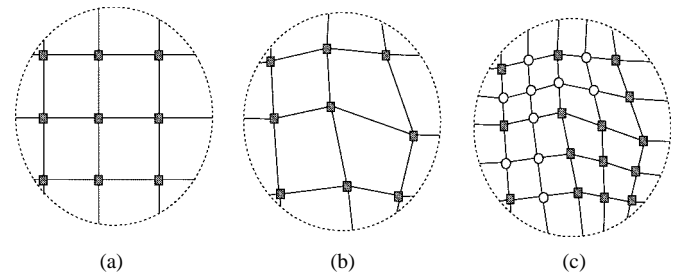Fig. 3. Illustration of the unstretched and stretched springs of a node.

Fig. 4. Allocation of nodes. (a) The initial quadrilateral mesh. (b) The mesh structure after spring energy minimization in the first hierarchic level. (c) The mesh after subdivision in the second level. The normal and floating nodes are denoted by squares and circles, respectively. The normal nodes in (c) are either inherited from the initial mesh in (b) or added when the intraelement feature energy is high and interpolation error is small.
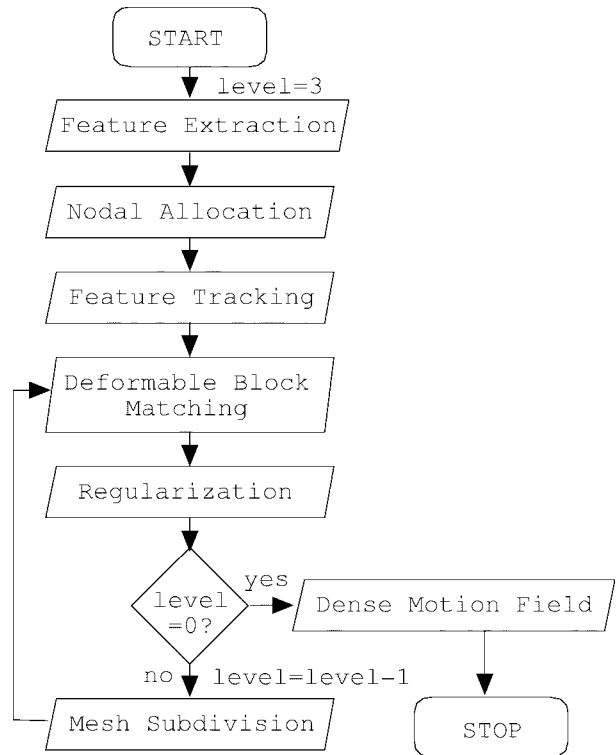

Fig. 5. Flow diagram of the mesh-based motion estimation algorithm.

constant can be used to control the degree of deformation of the initial regular grid.

The formulation of mesh generation in terms of potential energy can be used to determine a configuration of nodal positions. This is done by moving a node to a location of minimum nodal potential energy while fixing its neighboring nodes to their original locations. The movement of a node must be restricted so as not to produce a degenerate element. The easiest way to prevent the degeneration of an element is to limit the movement of a node within the boundary shown in Fig. 3. The nodes at the boundary may be fixed so as to retain a constant region of interest.

The mesh is incorporated within an hierarchic scheme in order to handle tissue displacements that are large compared to the size of grid element. In successive hierarchic levels after nodal allocation, each mesh element is subdivided recursively into four finer mesh elements until the number of subdivisions reaches an allowed value. Nodes are added to each element if its intraelement feature energy is above the threshold value t_f

$$\int_{D_m} C_f(\boldsymbol{x})\, d\boldsymbol{x} \geq t_f \tag{3}$$

and the interpolation error is below the threshold t_i

$$\int_{D_m} \left(f_k(\boldsymbol{x}) - f_{k+1}(\boldsymbol{x}+\boldsymbol{u})\right)^2 d\boldsymbol{x} \leq t_i \tag{4}$$

where f_k and f_{k+1} denote the intensity function of the reference and comparison frames, respectively, and $\boldsymbol{u}$ is the estimated motion vector. The threshold values, t_f and t_i are selected in such a way that only mesh elements with high intraelement feature energy and low speckle decorrelation undergo mesh division. The integration of feature energy and interpolation error over an element D_m is calculated easily using the Gauss quadrature formulation described in the Appendix. In order to ensure connectivity of the mesh structure, "floating" nodes are added to unassigned mesh elements. The position vectors of those nodes are uniformly interpolated from their neighboring nodes from the previous

level. Fig. 4 demonstrates the mesh structure of the first two hierarchic levels.

III. NONRIGID MOTION ESTIMATION

Fig. 5 shows a flow diagram of the implementation of our mesh-based speckle tracking method. The algorithm starts with an initialization step which extracts useful features, allocates nodes in the first hierarchical level and estimates initial tissue deformation by tracking successive frames of the composite feature energy map using the traditional block-matching technique. The motion estimation step consists of two distinct parts: deformable block matching and regularization.

The mesh design and motion estimation are implemented hierarchically in a unified framework. After the first pass, mesh elements are divided into finer elements. Position and motion vectors at newly added nodes are interpolated from the
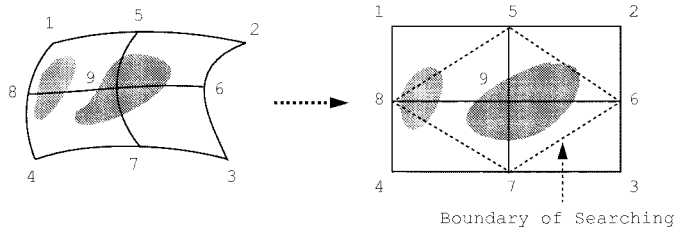
Fig. 6. Illustration of mapping of an irregular element to a regular parent element using a Lagrange shape function. The boundary of the allowed search region is marked using dashed lines. In this illustration, Node 9 is the target node.

existing nodes in a neighborhood. Deformable block matching and regularization procedures are executed again to update the estimates.

Production of a dense motion field in which motion vectors are obtained for all pixels in the image can be achieved using the inverse mapping of a four-node bilinear element [11] or the surface reconstruction method for sparsely distributed data points [12].

In the following, we shall describe the deformable block matching and regularization steps.

A. Block Matching Using Lagrange Elements

Deformable block matching is achieved by the use of a Lagrange shape function capable of representing second-order local motions so that an algorithm based on the assumption of rigidity can be extended to the situation of nonrigid motion estimation. The first step in deformable block matching is the mapping of an irregular mesh element D_m to a regular parent element $\tilde{D}_m$ as illustrated in Fig. 6. The parent element of the target node m is mapped from a nine-node macro-element using the Lagrange shape function (see the Appendix). The transformation not only compensates for deformation due to local nonrigid motion but also facilitates the manipulation of irregular mesh elements. Since the transformation of the mesh elements in the comparison frame accounts for tissue deformation, a normal block matching algorithm can be applied over the regular lattice of the parent element.

The parent mesh element is discretized to a 40×40 regular grid. The intensity value at each grid point is interpolated from the nodal values using (18). The discretization number of the parent element determines the potential sensitivity of the motion estimate, with the parent element resembling the search window in traditional block matching. With a 15×15 matching block at the target node in the reference parent element, the data block is used to compare this with another block positioned at a grid point in the comparison parent element. The search procedure seeks an optimal solution by minimizing the sum of the squared difference between the data blocks in the reference element $\Phi_{m,k}(s)$ and the comparison element $\Phi_{m,k+1}(s)$

$$\mathcal{E}_b = \tfrac{1}{2} \int_{\tilde{B}_m} \left(\Phi_{m,k+1}(s + \boldsymbol{d}) - \Phi_{m,k}(s) \right)^2 J_m \, \boldsymbol{ds}, \quad \forall m \in \mathcal{M}$$

$$(5)$$

where $\tilde{B}_m$ is the matching block, k is the image frame number, s is the index of discretized grid of the parent element and

J_m is the Jacobian of the element D_m. The displacement vector $\boldsymbol{d}$ is the estimated vector between the position of the target node and the best-matched position in the comparison parent element. Block matching is performed over reference and comparison parent elements of normal target nodes only, denoted by the set $\mathcal{M}$.

The estimate of the motion vector $\boldsymbol{u}(x)$ at the target node is given by

$$u_1 = \sum_{i=1}^{9} N_i x_1^*(i) - x_1$$

$$u_2 = \sum_{i=1}^{9} N_i x_2^*(i) - x_2 \qquad (6)$$

where N is the Lagrange shape function calculated with $\boldsymbol{d}$, i.e., $N(d_1, d_2)$, $\boldsymbol{x}$ is the position vector of the target node in the undeformed configuration, and $\boldsymbol{x}^*$ is the nodal position vector in the deformed configuration.

The deformed configuration of $\boldsymbol{u}$ is admissible only to a configuration that satisfies internal compatibility. The compatibility constraint is a nonzero Jacobian of the mesh element, satisfying $J_m > 0$. This implies that the comparison of matching blocks is restricted to the region marked by dashed lines in Fig. 6, thus, preventing the possibility of mesh degeneration in the comparison frame.

B. Regularization

As speckle tracking is an ill-posed inverse problem, maximum likelihood estimators such as sum squared difference are inadequate for accurate motion estimation. Regularization methods [13] are therefore needed. In mesh-based motion estimation, a conservative dynamic system is applied that has a potential energy and boundary conditions. In the dynamic mesh structure, changes in the shape or size of a mesh element resulting from an applied "imaging force" are considered to be associated with a strain energy. The imaging force is a similarity measure that preserves the intensity function at each node.

Although the strain energy formulation makes use of the theory of elasticity and involves the use of stress and strain tensors, the reader is cautioned against relating these parameters to the actual elasticity, stress, and strain within the imaged tissue. In our application, elastic theory is simply a convenient construct used to facilitate mesh regularization. Indeed, the selection of the elastic modulus in our model is completely arbitrary since a separate parameter α is used to control the degree of regularization applied. The possibility of using actual tissue elasticity for mesh regularization, perhaps using a dynamic iterative approach in which elasticity is calculated from the measured displacements and then used to refine the displacement values, is an intriguing one that is beyond the scope of this paper.

If the system is assumed to be conservative so that the associated work depends only on the difference between the undeformed and deformed configurations, the total potential energy of the dynamic mesh system can be expressed as

$$\mathcal{E} = \mathcal{E}_d + \mathcal{E}_e \qquad (7)$$

where $\mathcal{E}_d$ is the affinity energy based on the similarity measure of matching data blocks and $\mathcal{E}_e$ is the deformation energy of the mesh structure. The boundary conditions are the prescribed values of the nodes. Since the potential energy is computed using a nine-node macro-element (Lagrange element), the nodes at the boundary of the mesh are assigned with pre-scribed motion vectors obtained by traditional block matching methods.

The affinity energy $\mathcal{E}_d$ has the form

$$\mathcal{E}_d = \tfrac{1}{2}\left(u_m(\boldsymbol{x}) - \hat{u}_m(\boldsymbol{x})\right)^2 \quad \forall m \in \mathcal{M} \tag{8}$$

where $\hat{u}_m(\boldsymbol{x}$ is the motion vector estimated by deformable block matching at the normal nodes (denoted by $\mathcal{M}$). The deformation energy $\mathcal{E}_e$ is given by

$$\mathcal{E}_e = \tfrac{1}{2}\boldsymbol{U}^T \boldsymbol{K}_e U = \tfrac{1}{2} f_{\tilde{D}_m} \boldsymbol{e}^T \boldsymbol{E} e J_m ds, \quad \forall m \in \mathcal{M}, \mathcal{F} \tag{9}$$

where $\boldsymbol{e}$ is the strain, $\boldsymbol{K}_e$ is the stiffness matrix, $\boldsymbol{E}$ is a matrix of regularization parameters, and $\mathcal{F}$ is the set of all floating nodes (the strain energy constraint is applied to both normal and floating nodes). The values of strain are computed from the nodal displacements using the strain-displacement relation $\boldsymbol{e} = \boldsymbol{B}\boldsymbol{u}$. The matrix $\boldsymbol{B}$ is given as

$$\boldsymbol{B} = \boldsymbol{\Gamma}\boldsymbol{D}_N \tag{10}$$

where $\boldsymbol{\Gamma}$ is the inverse of the Jacobian matrix and $\boldsymbol{D}_N$ consists of the derivatives of the shape function of the Lagrange element (see the Appendix). Since the external load of similarity matching is applied over the 2-D imaging plane, an isotropic plane stress model can be used in formulating the matrix $\boldsymbol{E}$

$$\boldsymbol{E} = \frac{\alpha E}{1 - \nu^2}\begin{bmatrix} 1 & \nu & 0 \\ \nu & 1 & 0 \\ 0 & 0 & \dfrac{1-\nu}{2} \end{bmatrix} \tag{11}$$

where α is a regularization parameter, E is the Young's modulus [14], and ν is Poisson's ratio. For soft tissues, which are nearly incompressible, Poisson's ratio approaches 0.5 and, hence, it seems reasonable to apply the same value here. Since the regularization parameter α is assigned arbitrarily to control the degree of mesh deformation, the Young's modulus does not need to be determined for a homogeneous mesh structure with uniform stiffness. In the case of plane stress, strain has three components

$$\boldsymbol{e} = \begin{bmatrix} e_{x_1} \\ e_{x_2} \\ \gamma_{x_1 x_2} \end{bmatrix} = \begin{bmatrix} u_{1,1} \\ u_{2,2} \\ u_{1,2} + u_{2,1} \end{bmatrix} = \begin{bmatrix} \dfrac{\partial u_1}{\partial x_1} \\ \dfrac{\partial u_2}{\partial x_2} \\ \dfrac{\partial u_1}{\partial x_2} + \dfrac{\partial u_2}{\partial x_1} \end{bmatrix}. \tag{12}$$

C. Minimization Algorithm

The total potential energy in (7) can be written as

$$E = \tfrac{1}{2}\boldsymbol{U}[K]\boldsymbol{U} - \hat{U}U + c \tag{13}$$

where $[K] = [\boldsymbol{K}_e] + \boldsymbol{I}$, $\hat{\boldsymbol{U}}$ contains the nodal motion estimates by deformable block matching at the normal nodes only, and c contains the constant terms. The matrix $\boldsymbol{I}$, the identity matrix,

has zeros everywhere except that the diagonal elements corre-sponding to the normal nodes are set to one. The equilibrium configuration is found from the stationary value of the total potential energy

$$dE = \left([\boldsymbol{K}]\boldsymbol{U} - \hat{\boldsymbol{U}}\right) dU = 0. \tag{14}$$

When the configuration of nodes is in equilibrium, the total potential energy in (13) is at minimum for a stable system. Al-though the optimal configuration can be calculated by solving the linear equations of (14), the computation is formidable for a large number of nodes. Iterative methods should, therefore, be used instead. Many gradient descent algorithms can be used to minimize the energy function. The conjugate gradient descent (CGD) algorithm [15] is particularly well suited because of its effectiveness in using the gradient information of a quadratic equation such as (13). The gradients of $\mathcal{E}_d$ and $\mathcal{E}_e$ in (7) have the form

$$\frac{\partial \mathcal{E}_d}{\partial \boldsymbol{u}_m} = u_m(x) - \hat{u}_m(x), \quad \forall m \in \mathcal{M} \tag{15}$$

and

$$\frac{\partial \mathcal{E}_e}{\partial \boldsymbol{u}_m} = \frac{\partial \mathcal{E}_e}{\partial \boldsymbol{x}_m} = \int_{\tilde{D}_m} \boldsymbol{e} \boldsymbol{E} \boldsymbol{B} J_m \, ds, \quad \forall m \in \mathcal{M}, \mathcal{F}. \tag{16}$$

Readers are referred to [15] for a more complete explanation of the CGD algorithm.

IV. EXPERIMENTS AND RESULTS

In order to provide a suitable test of the reliability of the algorithm for speckle tracking, experiments were performed using synthetic images, computer-simulated rotation and com-pression, phantom experiments of translation and compression, and ultrasound images of muscle contraction. In the exper-iments that used synthetic images and computer simulations, the performance of the proposed algorithm with different types of nonrigid motion was tested. In the experiments in the phantom, the robustness of the algorithm in handling speckle decorrelation was demonstrated through the application simple controlled motions. The *in vivo* experiments involving muscle contraction evaluated the performance of the algorithm in a more realistic, although less controlled situation.

A. Simulation of Nonrigid Vibration

In the ideal case the accuracy of the speckle tracking algorithm should be tested in a situation in which the actual motion is known. Because of the difficulty in producing known nonrigid motion fields in biological tissues and of accurately measuring internal displacements by other means, we chose instead to simulate motion fields using finite element methods.

Fig. 7 illustrates a 2-D inhomogeneous simulated tissue phantom consisting of a hard inclusion embedded within a softer homogeneous material. The hard inclusion has a Young's modulus [14] of 40-k Pa and is embedded in a media with a Young's modulus of 10-k Pa. The dimension of the tissue phantom is 10 cm × 10 cm. The inclusion is a square-shaped region of dimension 2 cm × 2 cm. A sinusoidal force was applied along the plane of symmetry and a finite element

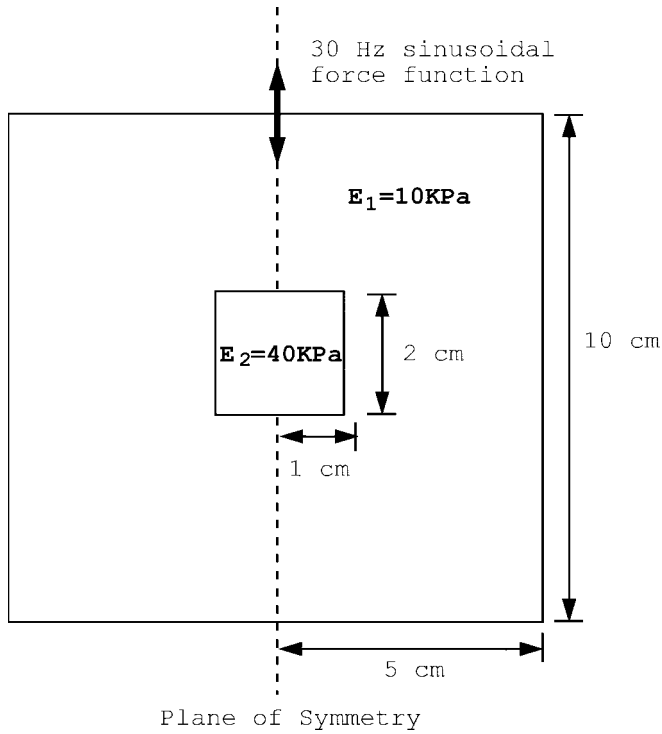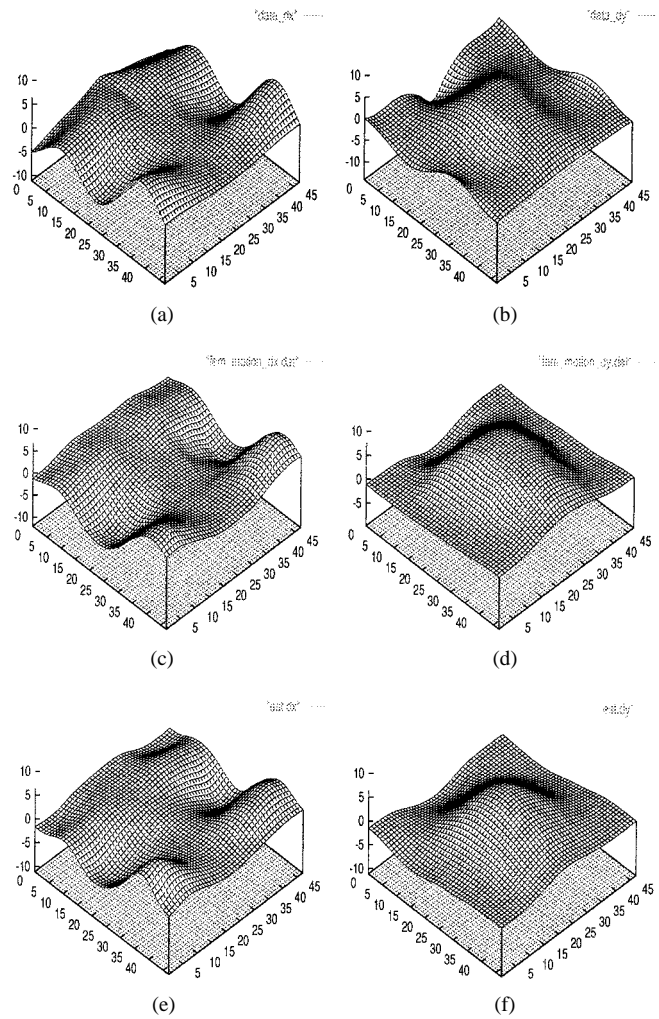Fig. 7. Parameters used in the FEM simulation of tissue motion.

Fig. 8. Surface plots of the motion components showing mesh-based motion tracking results of FEM simulation data: (a) actual motion u_1, (b) actual motion u_2, (c) reconstructed dense motion field u_1, (d) reconstructed dense motion field u_2, (e) reconstructed dense motion field u_1 based on noisy images (SNR = 10 dB), and (f) reconstructed dense motion field u_2 based on noisy images (SNR = 10 dB). The Z axis represents motion amplitude, while X and Y axes represent the spatial coordinates.

analysis software package, MSC/NASTRAN (The MacNeal-Schwendler Corp., Los Angeles, CA) was used to simulate the nonrigid tissue motion [16].

Ultrasound image sequences of speckle patterns were simulated using Rayleigh statistics. A second speckle image was mapped from the first image using the tissue motion at a finite time delay, simulated by the finite element analysis software. Warping of speckle pattern rather than the tissue scattering function, however, eliminates the effects of speckle decorrelation.

Fig. 8 shows the surface plots of the horizontal u_1 and vertical u_2 components of the motion vector field. Surfaces plots (a) and (b) are the actual motion components generated by the finite element analysis software. Plots (c) and (d) are the dense motion field reconstructed from (a) and (b), respectively. To evaluate the performance of the algorithm in the presence of noise, the two image pairs were corrupted with Gaussian noise (SNR = 10 dB) and the motion vectors were then recomputed, as shown in plots (e) and (f).

From the results, it is demonstrated that the speckle tracking algorithm successfully tracked the nonrigid motion field, even under noisy conditions. The mean squared tracking errors [8] in pixels for noise-free and noisy images were 0.73 and 1.23, respectively. These errors were small compared to the maximum motion amplitude (6.2 pixels). It can be noted that, although the basic form of the estimated motion matches that of the actual motion, the algorithm does not track motion as accurately along the image boundary as in the center. This is due to two reasons. First, the nodal motion vectors along the image boundary have prescribed values obtained by traditional block matching which does not take tissue deformation into account. Second, the regularization parameter α and Young's

modulus E have a profound effect on the smoothness of the estimated motion field. While the degree of smoothness in the hard inclusion seems to be adequate, the motion field in the soft surrounding region is over-constrained.

A variable parameter adaptive to the elastic properties of the tissues may be useful to control the degree of smoothness in different physical regions. However, this is beyond the scope of this paper. For an homogeneous tissue medium, prescribed E need not be computed since α is a user-supplied control parameter. Increasing the value of α would be expected to increase motion smoothness at the expense of motion detail, whereas decreasing α can be expected to increase the likelihood of incorrect estimates.

B. Simulation of Rotation and Compression

Both rotational (5° clockwise) and compressional (10% vertical compression and 10% horizontal expansion) motion fields were used to test the performance of the mesh-based speckle tracking algorithm. Ultrasound image sequences were
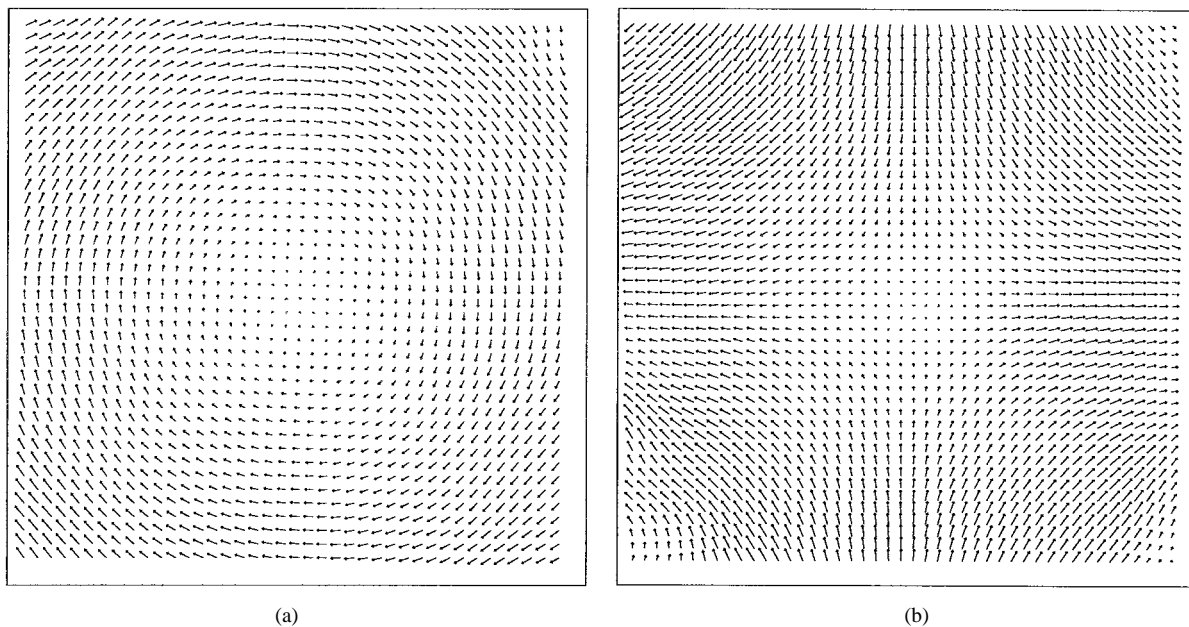
Fig. 9.   Dense motion vector field of mesh-tracking results of simulated (a) rotation and (b) compression.

created by warping a Rayleigh-governed envelope-detected speckle image into another image frame using the simulated motion fields. The ultrasonic frequency in the simulation model is 5 MHz and the pixel to meter ratio is 6800. The region of interest of the rotational motion field was 195×195 pixels (2.87×2.87 cm^2) and that of the compressional motion field was 120×120 (1.76×1.76 cm^2).

Fig. 9 shows the motion vector diagrams of the tracking results. The tracking errors in pixels are 0.70 and 0.62 for rotation and compression, respectively.

C. Phantom Experiments

Translation and compression experiments were performed using a gelatin-based tissue-mimicking phantom of dimension 14.5 cm $\times$ 9.8 cm $\times$ 5.6 cm. Fig. 10 illustrates the experimental setup. Ultrasonic echo data was collected using a GE LOGIQ 700 scanner with the Extend package. The Extend package transferred 8-b B-mode digital ultrasound data directly from the commercial scanner LOGIQ 700 console to an on-board computer for later transfer to an SGI O$_2$ workstation (Silicon Graphics, Inc., Mountain View, CA). A linear-array ultrasound transducer (5 MHz), fixed firmly to a 3-D manipulator, was placed on the top of the phantom. A 4 cm $\times$ 3 cm imaging region, corresponding to 300×200 pixels, was selected.

1) Translation: In the translation experiment, the transducer was linearly translated in 5 mm ($\pm$ 0.1 mm) lateral increments. Each increment of translation corresponded to 3.76 pixels. A mesh, with a size of 128×128 pixels and a total of 256 nodes, was imposed onto the image frames for motion tracking.

Fig. 11 shows the 2-D dense motion field tracking result. The mean-squared tracking error and PSNR were 0.141 pixels (0.1302 pixels in u_1 motion component and 0.011 pixels in u_2 component) and 71.98 dB, respectively. For translation motion, the tracking accuracy reaches 96.28% in this experiment.
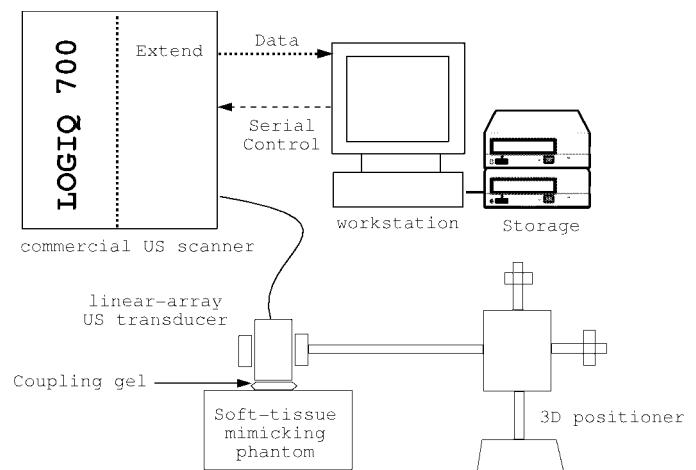

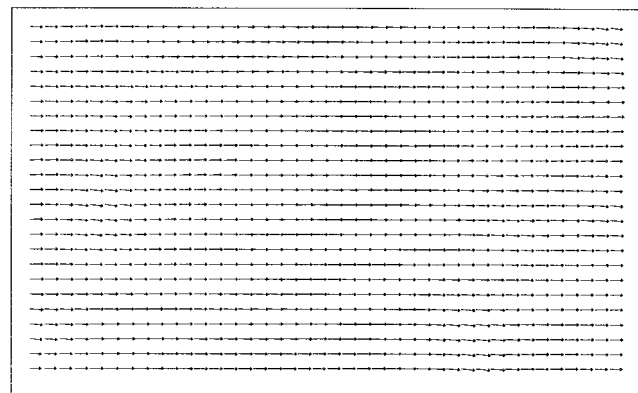Fig. 10.   Diagram of the experimental setup.

Fig. 11.   Dense motion vector field resulting from the translation experiment.

2) Compression: In this experiment, an homogeneous tissue-mimicking gelatin phantom was placed between two plates. The top plate acted as a tissue compressor. The degree
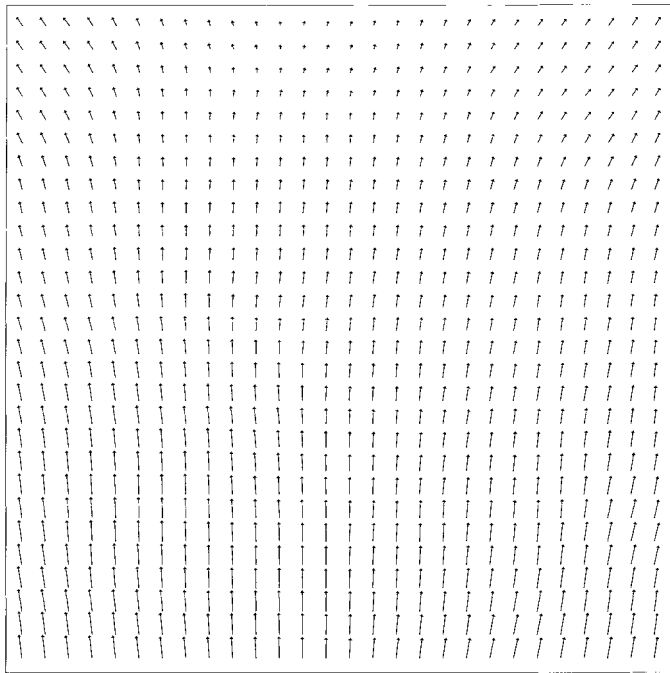
Fig. 12. Dense motion vector field resulting from the compression experiment.
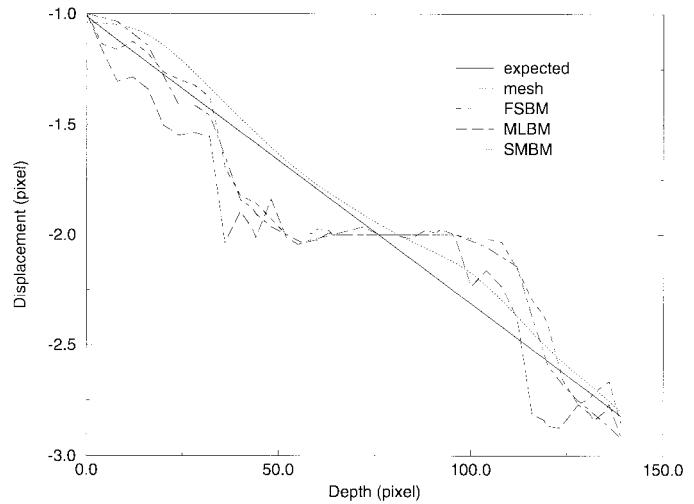

Fig. 13. Plot of vertical motion component of phantom compression using feature adaptive mesh (mesh), full-scale (FS), multilevel (ML), and smooth motion (SM) block matching (BM) methods.
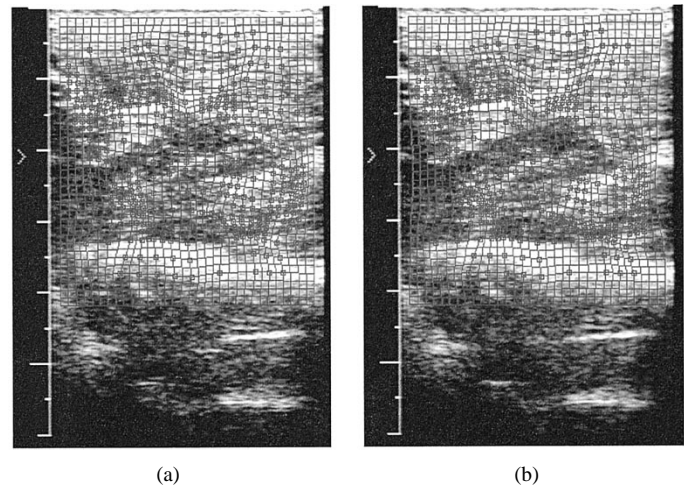

Fig. 14. Illustration of two image frames of a muscle contraction sequence superimposed with (a) deformed and (b) undeformed mesh structures. The normal nodes are marked by squares. The first figure, with labels provided for the different regions, can be found in [8]. At first, no motion may be evident to the reader because the motions are small and quantized to integer pixel values. More careful observation, however, particularly along the mesh boundaries on the right, will reveal a difference between the two image frames.

of compression was controlled using a 3-D manipulator. In each compression step, the top plate moved downward by 0.6 mm. A transducer was placed within an opening in the bottom plate underneath the phantom. The top plate was restored to its original position when it could move down no further.

A 240×240 mesh (640 nodes) was used for mesh-based tracking. A dense motion vector field of the phantom compression results is shown in Fig. 12. Fig. 13 plots the u_2 motion component (averaged over ten-pixel columns along the center) versus depth. The resulting curve, roughly a straight line, agrees with the expectation of constant strain caused by a uniformly distributed stress in an homogeneous medium. The expected displacement curve is plotted as a solid straight line. For comparison, the displacement curves of previously used block-based algorithms [8] derived from the same image frames are also given. The mean squared tracking error in pixels of the mesh-based tracking result is 0.005, while those of block-based algorithms (FSBM, MLBM, and SMBM) are 0.034, 0.047, and 0.031, respectively. From the displacement curves, the quantization effect is obvious for the block-based algorithms. In this experiment, the mesh-based tracking algorithm significantly outperformed the block-based algorithms.

D. Muscle Contraction Experiment

In order to evaluate the algorithm in living tissue, a complex muscle motion experiment was performed. Although it was not possible to measure the true motion of the muscles independently of speckle tracking, we felt that the data obtained could provide important insights into the ability of the algorithm to handle nonrigid motion fields from clinical data.

The ultrasound image sequence was obtained by scanning the forearm from a single subject in cross-section using a 7-MHz linear array ultrasound scanner (Acuson, Mountain

View, CA) at a frame rate of 16 Hz. The resulting image (Fig. 14) demonstrates a bright region at the bottom, the *ulna*, on top of which are the forearm flexor muscles, blood vessels and nerves. Two groups of muscles, the flexor *digitorum superficialis* at the top right and the *flexor digitorum profundus* in the middle right are of interest in this experiment, as these are the muscles responsible for finger flexion. The subject was asked to bend his middle finger against resistance so as to contract these two muscles to a greater degree than the surrounding musculature.

Two frames of the muscle contraction sequence, upon which the mesh structures have been superimposed, are illustrated in Fig. 14. It was observed that the mesh nodes migrated to the locations of more structural speckle patterns and the vicinities of differentiated tissue structures were packed more densely
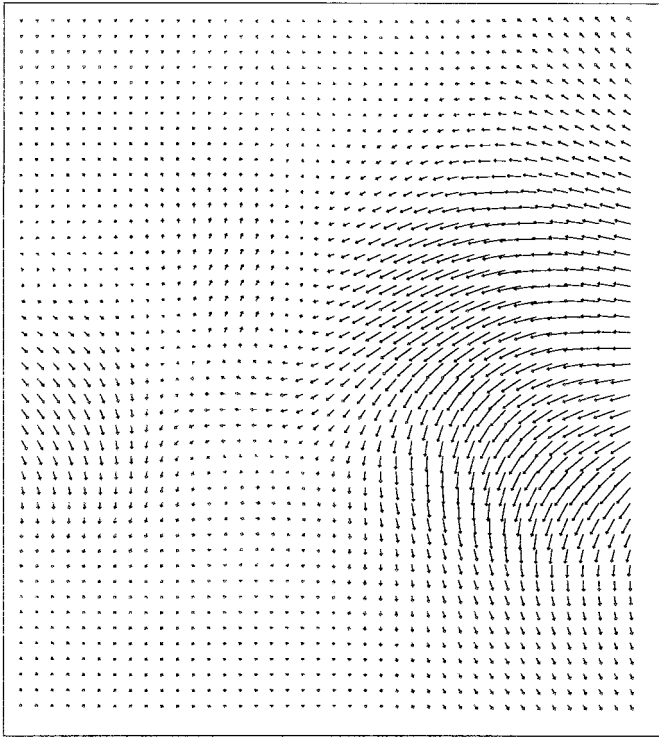
Fig. 15.   Dense motion vector field of muscle contraction.

with nodes. The dense motion vector field is plotted in Fig. 15. From the motion vector field, it is easy to differentiate among the muscle groups involved in finger contraction. Although the actual displacements in various regions of the image are not available, the estimated motion field is in agreement with the expected anatomical changes.

V. SUMMARY AND DISCUSSION

In this paper an adaptive mesh has been proposed for nonrigid tissue motion estimation from ultrasound image sequences. A deformable blocking matching algorithm has been developed which takes into consideration both similarity measures and strain energy caused by mesh deformation. By partitioning an image domain into polygonal elements, the mesh constitutes an efficient representation of image intensity information. The treatment of speckle tracking using a mesh structure has distinct merit in visualizing tissue motion. Manipulation of irregular mesh elements is aided by a wealth of well-established mathematical tools in finite element analysis.

Recently, mesh-based motion modeling has also been successfully applied in digital video processing. A multiresolution representation called the quadtree spline has been proposed by Szeliski and Shum [17] to describe the motion field as a collection of connected patches of varying sizes adaptive to the complexity of the motion. A preconditioned conjugated gradient is used to solve for the motion estimates, regulated by the smooth function of a coarse-to-fine spline control grid. Toklu *et al.* [18] proposed a mesh-based motion model under the mild deformation assumption to track the motion of deformable objects such as a flying flag. Wang and Lee [11] used an iterative gradient-based nodal motion vector esti-

mation method based on a deformable mesh that takes image gradient information into account. A closed-form technique has been suggested by Altunbasak and Tekalp [19] to compute the optimal motion vector at each node while preserving mesh connectivity constraints.

Our mesh-based speckle tracking algorithm differs from these methods in many different ways. First, both mesh design and motion estimation in our algorithm are specifically designed for speckle tracking. The mesh serves as a superior framework for ultrasonic speckle tracking in that mesh nodes are allocated adaptively to anticipated stable speckle patterns. Second, the ability of an algorithm to describe higher-order local motion is ultimately limited by the type of mesh elements used in mesh tracking. We employed a nine-node Lagrange element with deformable block matching to approximate local motion to the second order. Finally, for the matching-based methods, search procedures for optimal motion estimation within irregular mesh elements are cumbersome to implement. We implemented a search process over the regular parent elements, as opposed to the irregular mesh elements.

The extension of a block matching algorithm to nonrigid motion estimation is an important contribution of this paper. The preference of using the Lagrange element over other higher-order elements is due to its simplicity as an extension of the four-node bilinear element and its ability to exhibit all possible deformations of a quadratic element. Elements that are higher than second-order could describe nonrigid motion fields better still, but at the expense of increased complexity.

The mapping of an irregular element to a regular parent element offers many advantages in motion tracking. In traditional block matching, subpixel motion estimates are obtained by interpolation. However, this technique is difficult to implement with an irregular lattice. By discretizing the parent elements, finer motion estimates can be obtained by discretizing to a finer grid. Moreover, instead of checking for degenerate cases in irregular elements, it is much easier to impose the compatibility constraint by restricting nodal movement in the regular parent element.

Implementation of the algorithm in an hierarchic scheme offers a solution to problems related to measurement of local tissue motion. A multilevel block matching algorithm for speckle tracking that has previously been introduced [8] is adapted to the hierarchic structure of the mesh implementation. The nodal motion vectors from each hierarchic level are passed on to the successive levels such that the final estimates will consist of the sums of the motion estimates from all levels. The algorithm estimates coarse motion fields using large mesh elements in the initial level and successively passes the result to the subsequent levels, each of which uses smaller mesh elements than the previous level. This strategy helps to reduce the problems of motion ambiguities and spatial aliasing in speckle tracking. Since each level has a finer grid spacing than the last, initial estimates of the additional nodes are interpolated from the existing nodes in the surrounding neighborhood, helping to accelerate convergence of the minimization process.

Last but not the least, the connectivity of the mesh and the strain energy constraint effectively reduce the effect of
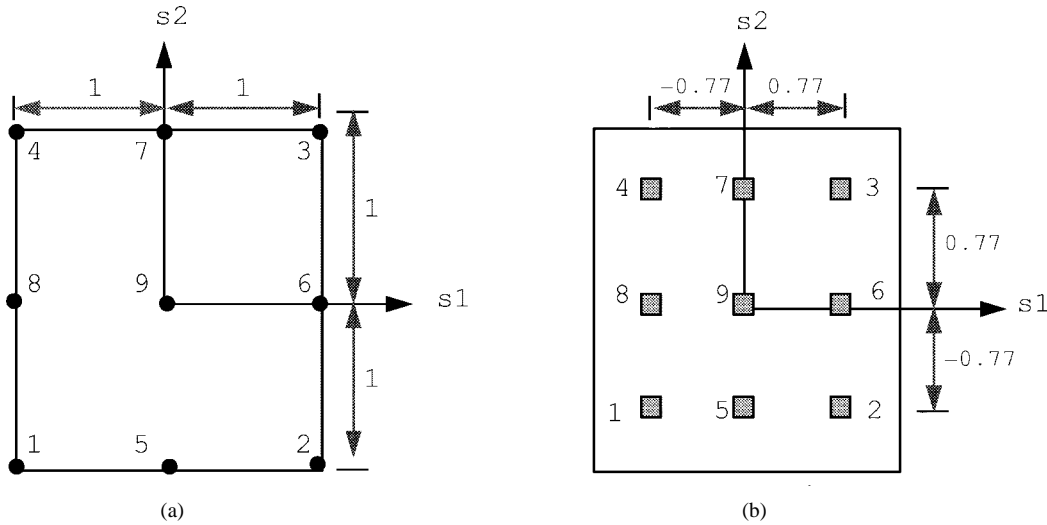
Fig. 16.   Illustration of (a) nine-node Lagrange parent element and (b) Gauss point locations in the Lagrange element.

speckle decorrelation caused by nonuniform movement of scatterers and out-of-plane motion. This strategy also handles the problem of low SNR in ultrasound images by aligning the local data of weak estimates to those of strong estimates. One potential disadvantage of using the strain energy constraint is a blurring effect at motion boundaries. Fortunately, motion continuity is still valid even at the boundaries of tissues with differing properties because the stress function is also continuous. In the experiment of a simulated motion field in an inhomogeneous medium, the tissue motion was continuous across the boundary of the hard inclusion and its surrounding soft medium. However, motion fields may be discontinuous at the boundaries under conditions of slip. This is the case at the boundaries of different groups of muscles. Further investigation is needed into discontinuity-adaptive methods for motion tracking of biological tissues.

APPENDIX
FINITE ELEMENT ANALYSIS

This section gives an overview of FEA techniques employed in the formulation of the proposed algorithm. Readers unfamiliar with FEA techniques are referred to [20]. Our approach involves making use of the shape function obtained from a finite element representation of an irregular mesh grid. As such, our method differs from more conventional approaches in which FEA is used to represent a system of equations to calculate the displacements resulting from an applied external load (forward problem) or to derive the underlying tissue properties from known displacements (inverse problem).

The mesh is designed to approximate a function over a continuous domain. The function within each mesh element is interpolated from its nodal values. Such interpolation is denoted by a shape function $\boldsymbol{N}$. The shape function of a nine-node Lagrange element, illustrated in Fig. 16(a), is given by

$$N_1 = \tfrac{1}{4}(1 - s_1)(1 - s_2) - \tfrac{1}{2}N_5 - \tfrac{1}{2}N_8 + \tfrac{1}{4}N_9$$
$$N_2 = \tfrac{1}{4}(1 + s_1)(1 - s_2) - \tfrac{1}{2}N_5 - \tfrac{1}{2}N_6 + \tfrac{1}{4}N_9$$

$$N_3 = \tfrac{1}{4}(1 + s_1)(1 + s_2) - \tfrac{1}{2}N_6 - \tfrac{1}{2}N_7 + \tfrac{1}{4}N_9$$
$$N_4 = \tfrac{1}{4}(1 - s_1)(1 + s_2) - \tfrac{1}{2}N_7 - \tfrac{1}{2}N_8 + \tfrac{1}{4}N_9$$
$$N_5 = \tfrac{1}{2}(1 - s_1^2)(1 - s_2) - \tfrac{1}{2}N_9$$
$$N_6 = \tfrac{1}{2}(1 + s_1)(1 - s_2^2) - \tfrac{1}{2}N_9$$
$$N_7 = \tfrac{1}{2}(1 - s_1^2)(1 + s_2) - \tfrac{1}{2}N_9$$
$$N_8 = \tfrac{1}{2}(1 - s_1)(1 - s_2^2) - \tfrac{1}{2}N_9$$
$$N_9 = (1 - s_1^2)(1 - s_2^2) \tag{17}$$

where s_1 and s_2 are intrinsic coordinates in the parent element. The shape function has a value of unity at the node to which it is related. It also has the property that the sum at any point within an element is equal to unity. The efficiency of any particular element type will depend on how well the shape function is capable of representing the local displacement field. The shape function of the Lagrange element is capable of representing second-order nonrigid motion.

The initial step in finite element analysis is the unique description of an unknown function within each irregular element in terms of the values of this function at the nodal points of the element. Each irregular element, D_m, can be thought of as being deformed from a regular parent element $\tilde{D}_m$. Both the displacements and coordinates can be interpolated from the nodal values using the same shape function. Coordinates x_1 and x_2 within an irregular element D_m are defined by

$$x_1 = \sum_{i=1}^{9} N_i \tilde{x}_1(i) \quad \text{and} \quad x_2 = \sum_{i=1}^{9} N_i \tilde{x}_2(i). \tag{18}$$

Similarly, displacements u_1 and u_2 are given by

$$u_1 = \sum_{i=1}^{9} N_i \tilde{u}_1(i) \quad \text{and} \quad u_2 = \sum_{i=1}^{9} N_i \tilde{u}_2(i) \tag{19}$$

where $\tilde{u}_1$ and $\tilde{u}_2$ are displacements in the parent element.

The forward transformation of an arbitrary irregular element into a regular one is important in manipulating the mesh elements. The properties of the transformation are investigated

by its Jacobian matrix $\boldsymbol{J}$

$$\boldsymbol{J} = \begin{bmatrix} J_{11} & J_{12} \\ J_{21} & J_{22} \end{bmatrix} = \begin{bmatrix} \sum N_{i,s_1}\tilde{x}_1(i) & \sum N_{i,s_2}\tilde{x}_2(i) \\ \sum N_{i,s_2}\tilde{x}_1(i) & \sum N_{i,s_1}\tilde{x}_2(i) \end{bmatrix} \tag{20}$$

which contains the derivatives of the shape function. The derivative matrix of the shape function is given by

$$\boldsymbol{D}_N = \begin{bmatrix} N_{1,s_1} & N_{2,s_1} & N_{3,s_1} & N_{4,s_1} & N_{5,s_1} \\ N_{1,s_2} & N_{2,s_1} & N_{3,s_2} & N_{4,s_2} & N_{5,s_2} \end{bmatrix}$$
$$\begin{bmatrix} N_{6,s_1} & N_{7,s_1} & N_{8,s_1} & N_{9,s_1} \\ N_{6,s_2} & N_{7,s_2} & N_{8,s_2} & N_{9,s_2} \end{bmatrix}. \tag{21}$$

The determinant of the Jacobian matrix $J = \det[\boldsymbol{J}]$ is regarded as a scale factor that is the ratio of the area $dx_1 dx_2$ to $ds_1 ds_2$. The coordinate transformation is unique and invertible if and only if its Jacobian is nonzero everywhere. The Jacobian must be positive for every mesh element. The inverse matrix $\boldsymbol{\Gamma}$ of $\boldsymbol{J}$ is given by

$$\boldsymbol{\Gamma} = \boldsymbol{J}^{-1} = \frac{1}{J} \begin{bmatrix} J_{22} & -J_{12} \\ -J_{21} & J_{11} \end{bmatrix}. \tag{22}$$

The determinant of the Jacobian matrix plays an important role in the numerical integration of integrals. In finite element analysis, an integral is evaluated numerically based on the *Gauss quadrature* method, rather than analytically. The integration over an arbitrary element can be accomplished over the regular parent element by a change of variables, as

$$I = \int\int_{D_m} f_m(x)\, dx_1\, dx_2$$
$$= \int_{-1}^{1}\int_{-1}^{1} f_m(s) J_m\, ds_1\, ds_2. \tag{23}$$

The right-hand side of (23) is calculated using the Gauss quadrature rule which states that, for a function ϕ, numeric integration can be approximated as

$$I \approx \frac{25}{81}(\phi_1 + \phi_2 + \phi_3 + \phi_4) + \frac{40}{81}(\phi_5 + \phi_6 + \phi_7 + \phi_8)$$
$$+ \frac{64}{81}\phi_9 \tag{24}$$

where the function $\phi = \phi(s_1, s_2)$ is estimated at one of the Gauss points illustrated in Fig. 16(b).

REFERENCES

[1] I. A. Hein and W. D. O'Brien, "Current time-domain methods for assessing tissue motion by analysis from reflected ultrasound echoes—A review," *IEEE Trans. Ultrason., Ferroelect., Freq. Contr.*, vol. 40, pp. 84–102, 1993.

[2] G. E. Mailloux, F. Langlois, P. Y. Simard, and M. Bertrand, "Restoration of the velocity field of the heart from two-dimensional echocardiograms," *IEEE Trans. Med. Imag.*, vol. 8, pp. 143–153, Apr. 1989.

[3] G. E. Trahey, S. M. Hubbard, and O. T. von Ramm, "Angle independent ultrasonic blood flow detection by frame-to-frame correlation of b-mode images," *Ultrason., Ferroelect., Freq. Contr.*, vol. 35, no. 1, pp. 34–44, 1988.

[4] S. F. Levinson, F. Yeung, W. Walker, and G. E. Trahey, "A sonoelasticity imaging display for 2-d speckle tracking," *Ultrason. Imag.*, vol. 16, pp. 38, 1994.

[5] F. Kallel, M. Bertrand, and J. Meunier, "Speckle motion artifact under tissue rotation," *IEEE Trans. Ultrason., Ferroelect., Freq. Contr.*, vol. 41, pp. 105–122, Jan. 1994.

[6] K. K. Shung, M. B. Smith, and B. Tsui, *Principles of Medical Imaging.* New York: Academic, 1992.

[7] R. F. Wagner, S. W. Smith, J. M. Sandrik, and H. Lopez, "Statistics of speckle in ultrasound b-scans," *IEEE Trans. Sonics Ultrason.*, vol. SU-30, pp. 156–163, May 1983.

[8] F. Yeung, S. F. Levinson, and K. J. Parker, "Multi-level and motion model-based ultrasonic speckle tracking algorithms," *Ultrasound in Med. Biol.*, vol. 24, no. 3, pp. 427–441, 1998.

[9] A. C. Bovik, M. Clark, and W. S. Geisler, "Multichannel texture analysis using localized spatial filters," *IEEE Trans. Pattern Anal. Machine Intell.*, pp. 55–73, Dec. 1990.

[10] E. P. Simoncelli, W. T. Freeman, E. H. Adelson, and D. J. Heeper, "Shiftable multi-scale transforms," *IEEE Trans. Inform. Theory*, vol. 38, pp. 587–607, Mar. 1992.

[11] Y. Wang and O. Lee, "Use of two-dimensional deformable mesh structures for video coding," *IEEE Trans. Circuits Syst. Video Technol.*, vol. 6, pp. 636–659, Dec. 1996.

[12] F. Yeung, "Motion estimation and analysis of ultrasound image sequences," Ph.D. dissertation, Univ. Rochester, Rochester, NY 1998.

[13] T. Poggio, V. Torre, and C. Koch, "Computational vision and regularization theory," *Nature*, vol. 317, no. 26, pp. 314–319, 1985.

[14] Y. C. Fung, *First Course in Continuum Mechanics,* 3rd ed. Englewood Cliffs, NJ: Prentice-Hall, 1994.

[15] G. H. Golub and C. F. van Loan, *Matrix Computations*, 3rd ed. Baltimore, MD: Johns Hopkins Univ. Press, 1996.

[16] K. Blakely, *MSC/NASTRAN Basic Dynamic Analysis: User's Guide.* Los Angeles, CA: MacNeal-Schwendler, 1993.

[17] R. Szeliski and H. Shum, "Motion estimation with quadtree splines," *IEEE Trans. Pattern Anal. Machine Intell.*, vol. 18, pp. 1199–1210, Dec. 1996.

[18] C. Toklu, A. T. Erdem, M. I. Sezen, and A. M. Tekalp, "Tracking motion and intensity variations using hierarchical 2-D mesh modeling for synthetic object transfiguration," *Graph. Models, Image Processing*, vol. 58, no. 6, pp. 553–573, Nov. 1996.

[19] Y. Altunbasak and A. M. Tekalp, "Occlusion-adaptive, content-based mesh design and forward tracking," *IEEE Trans. Image Processing*, vol. 6, pp. 1270–1280, Sept. 1997.

[20] R. D. Cook, D. S. Malkus, and M. E. Plesha, *Concepts and Applications of Finite Element Analysis.* New York: Wiley, 1989.